10-2016

Separability Analysis of Sentinel-2A Multi-Spectral Instrument (MSI) Data for Burned Area Discrimination

Haiyan Huang
South Dakota State University, haiyan.huang@sdstate.edu

David P. Roy
South Dakota State University, david.roy@sdstate.edu

Luigi Boschetti
University of Idaho

Hankui Zhang
South Dakota State University, hankui.zhang@sdstate.edu

Lin Yan Dr.
South Dakota State University, lin.yan@sdstate.edu

See next page for additional authors

Recommended Citation

Authors

Haiyan Huang, David P. Roy, Luigi Boschetti, Hankui Zhang, Lin Yan Dr., Sanath Sathyachandran Kumar, Jose Gomez-Dans, and Jian Li

Article

Separability Analysis of Sentinel-2A Multi-Spectral Instrument (MSI) Data for Burned Area Discrimination

Haiyan Huang [1],*, David P. Roy [1], Luigi Boschetti [2], Hankui K. Zhang [1], Lin Yan [1], Sanath Sathyachandran Kumar [1], Jose Gomez-Dans [3,4] and Jian Li [1]

[1] Geospatial Sciences Center of Excellence, South Dakota State University, Brookings, SD 57007, USA; david.roy@sdstate.edu (D.P.R.); hankui.zhang@sdstate.edu (H.K.Z.); lin.yan@sdstate.edu (L.Y.); sanath.kumar@sdstate.edu (S.S.K.); jian.li@sdstate.edu (J.L.)

[2] Department of Natural Resources and Society, College of Natural Resources, University of Idaho, Moscow, ID 83844, USA; luigi@uidaho.edu

[3] NERC National Centre for Earth Observation (NCEO), UCL Geography, Gower Street, London WC1E 6BT, UK; j.gomez-dans@ucl.ac.uk

[4] Department of Geography, University College London, Gower Street, London WC1E 6BT, UK

* Correspondence: haiyan.huang@sdstate.edu; Tel.: +1-605-688-6406

Abstract: Biomass burning is a global phenomenon and systematic burned area mapping is of increasing importance for science and applications. With high spatial resolution and novelty in band design, the recently launched Sentinel-2A satellite provides a new opportunity for moderate spatial resolution burned area mapping. This study examines the performance of the Sentinel-2A Multi Spectral Instrument (MSI) bands and derived spectral indices to differentiate between unburned and burned areas. For this purpose, five pairs of pre-fire and post-fire top of atmosphere (TOA reflectance) and atmospherically corrected (surface reflectance) images were studied. The pixel values of locations that were unburned in the first image and burned in the second image, as well as the values of locations that were unburned in both images which served as a control, were compared and the discrimination of individual bands and spectral indices were evaluated using parametric (transformed divergence) and non-parametric (decision tree) approaches. Based on the results, the most suitable MSI bands to detect burned areas are the 20 m near-infrared, short wave infrared and red-edge bands, while the performance of the spectral indices varied with location. The atmospheric correction only significantly influenced the separability of the visible wavelength bands. The results provide insights that are useful for developing Sentinel-2 burned area mapping algorithms.

Keywords: Sentinel-2; fire; burned area; separability analysis

1. Introduction

Satellite data have been used to systematically monitor fire globally at coarse spatial resolution, using algorithms that detect the location of active fires at the time of satellite overpass, and using burned area mapping algorithms that map the spatial extent of the areas affected by fires [1–7]. There is a need for moderate spatial resolution burned area products at regional to global scale that to date has only been partially met [8]. The launch of Sentinel-2A and the forthcoming launch of the Sentinel-2B satellite that carry the Multi Spectral Instrument (MSI) [9] provide the opportunity for moderate spatial resolution burned area mapping. Combined, the Sentinel-2A and -2B systems will provide multi-spectral global coverage up to every 5 days. The MSI has 13 spectral bands ranging

from 0.433 µm to 2.19 µm; four 10 m visible and near-infrared bands, six 20 m red edge, near-infrared (NIR) and short wave infrared (SWIR) bands, and three 60 m bands for characterizing aerosols, water vapor and cirrus clouds [9]. The MSI bands are similar to the Landsat-8, SPOT-6 and SPOT-7 bands and so include wavelengths that are suitable for burned area discrimination. Burned areas are characterized by deposits of charcoal and ash, and also by the removal of vegetation and alteration of the vegetation structure that sometimes reveal the vegetation understory and/or soil [10–12]. The fire behavior controls the severity of fire effects including the degree and parts of the vegetation structure that burned, the amount of charcoal and ash deposition, the combustion completeness, and the size and spatial distribution of the burning [13,14]. The persistence of the charcoal and ash signal depends on rates of dissipation by wind and rain and may be controlled by the unburned fuel load and structure [15,16]. Post-fire the vegetation may regrow, at rates dependent on the site primary productivity and environmental factors and have a phenological signal that complicates burned area detection [17–20]. Consequently, the reflectance over a burned area may have considerable variation in space and time as the spectral characteristics of unburned and burned areas change.

In general, NIR and shortwave-infrared wavelengths have been found to provide stronger burned area discrimination than visible wavelengths, and most burned area mapping algorithms are based on detecting decreased reflectance at these wavelengths. However, in some cases reflectance can increase due to the exposure of highly reflective soil and white ash deposition [12,21,22]. In addition, some surface changes not associated with fire, such as shadows or agricultural harvesting, may induce similar spectral changes and depending on the algorithm and wavelengths used may cause false burned area detection [2,23]. Visible wavelengths are not generally suitable for burned area detection because they are more sensitive to atmospheric contamination than longer wavelength bands and in particular are sensitive to smoke aerosols that are difficult to atmospherically correct [24,25]. A large number of researchers have used spectral indices to map burned areas. Ideally, if a spectral index is appropriate to detect the physical change of interest, then there is a simple relationship between the change and the direction of the change displacement in spectral feature space [26]. However, burned area spectral indices have often been designed quite empirically, for example, by considering every possible combination of bands and a variety of non-linear band transformations [27–31]. Although spectral indices may produce good burned area discrimination for a particular location and time they may not perform well elsewhere. Commonly, indices based on spectral band ratios, usually of NIR and SWIR wavelengths that are less sensitive to atmospheric contamination, are used. The ratio formulation reduces first order bi-directional reflectance and solar zenith induced reflectance variations [32]. Notably, the normalized burn ratio (NBR), computed as the difference between NIR and SWIR reflectance divided by their sum has been used widely for burned area mapping [33–36].

The purpose of this research is to investigate which Sentinel-2A MSI bands provide greater burned area discrimination. Pairs of largely cloud-free Sentinel-2A images, which were sensed 10 or 20 days apart were selected before and after visually identified fire events that produced evident burned areas at sites in tropical, sub-tropical, and boreal regions are examined. Both top of atmosphere and surface reflectance MSI data are examined. Parametric and non-parametric statistical techniques are used to quantify the spectral burned to unburned separability for different MSI bands and a select number of spectral indices.

2. Data and Pre-Processing

2.1. Sentinel-2 Images

Sentinel-2A MSI data are acquired in an approximately 290 km swath (20.6° field of view from an altitude of 786 km) with global coverage every 10 days [9]. The data are available as geolocated L1C top of atmosphere (TOA) products defined by splitting each MSI swath into fixed 109 × 109 km^2 tiles in the Universal Transverse Mercator (UTM) map projection. Pairs of predominantly cloud free L1C images acquired before and after major fire events were selected by comparison of the Sentinel-2A data

archive with the global daily Moderate Resolution Imaging Spectroradiometer (MODIS) 1 km active fire detection (MODIS Near Real-time Collection 6) available in the Fire Information for Resource Management System (FIRMS) web system [37]. Due to the sometimes rapid change in post-fire reflectance, attempts were made to ensure that only pairs of Sentinel-2 images acquired within the shortest interval, i.e., 10 days, apart were selected. However, this was not always possible due to cloud obscuration and Sentinel-2 data unavailability.

Pairs of images at five sites located in the Northern Territory, Australia; S.E Cambodia close to the Vietnam border; over the recent Fort McMurray fire in Alberta, Canada; in central Guinea; and in north central Colombia, were selected. The sites are in tropical, sub-tropical and boreal regions. No temperate sites were available because the first Sentinel-2A data became publicly available in November 2015, which was after the end of the main global temperate fire seasons [38]. The predominant land cover, as defined by the 2013 Collection 5.1 MODIS 500 m land cover product [39], over each site where unburned and burned pixels were analyzed is summarized in Table 1.

Table 1. Sentinel-2A Multi Spectral Instrument (MSI) L1C tile data used.

Site Location	L1C Tile ID	Acquisition Date 1	Acquisition Date 2	Predominant Vegetation Type
Australia, Northern Territory, near Fish River Block Gorge National Park	52LFK	10 April 2016	30 April 2016	Savannas
Cambodia, Kratié region, near Snoul	48PXU	7 January 2016	17 January 2016	Woody savannas
Canada, Alberta, Fort McMurray	12VVH	2 May 2016	12 May 2016	Evergreen needle leaf forest & Mixed forests
Guinea, Faranah Prefecture, Parc National du Haut Niger	29PLM	15 March 2016	25 March 2016	Woody savannas
Colombia, Casanare Department, northern side of the Rio Cravo Sur river	18NZL	17 January 2016	6 Feburary 2016	Savannas & Grassland

2.2. Sentinel-2 Image Pre-Processing

The Sentinel-2 L1C tiles have a complex structure. In particular, L1C tiles from the same MSI swath overlap spatially and a significant proportion may be defined in different UTM zones, i.e., in separate map projections, making reprojection and resampling of the data quite complicated [40,41]. However, in this study, only pairs of Sentinel-2A images sensed over the same L1C tile location were used, so no reprojection was necessary. The pixels for each image pair aligned within the Sentinel-2A geolocation performance specification of 12.5 m (3σ) [42].

The L1C products are provided as TOA reflectance. Atmospheric correction from TOA to surface reflectance is usually considered as a requirement for change detection applications [43]. The impact of the atmosphere is variable in space and time, and is dependent not just on the atmospheric constituents, but also on the surface reflectance. This is because multiple scattering of reflected radiation between the surface and the atmosphere introduces a dependency between the surface reflectance and the atmospheric contribution to the TOA reflectance [44,45]. Consequently, atmospheric correction of the data was undertaken as both the atmosphere and the surface changes between the Sentinel-2A acquisition dates. Simple image-wide atmospheric correction methods, such as the dark-object subtraction (DOS) method [46], are inappropriate for this study as smoke aerosols and pyrogenic emissions may be quite dynamic and spatially heterogeneous [24]. Consequently, the data were atmospherically corrected to surface reflectance using the recent radiative transfer based SEN2COR atmospheric correction software (Version 2.2.1, released 4 May 2016) run using the default parameter settings [47]. The SEN2COR code also produces a 20 m cloud product that was used qualitatively to help screen cloudy pixels. To date, no quantitative validation of the SEN2COR atmospheric correction and cloud mask product has been published. The Sentinel-2 has a 20.6° field of view (FOV) and so bi-directional reflectance effects (due to viewing and solar geometry variations and surface reflectance

anisotropy), which are present in similar spatial resolution and smaller field of view SPOT [48] and Landsat [49] data are likely to be present. However, bi-directional reflectance effects were not corrected for in this study.

2.3. Study Spectral Bands and Indices

The Sentinel-2A MSI has 13 spectral bands covering the spectral range 440–2180 nm, with 10 m, 20 m and 60 m pixels (Table 2). In this study the three 60 m bands (b01, b09 and b10) were not used due to their coarse spatial resolution and because they are specific to atmospheric characterization and not land surface monitoring. The remaining ten bands were selected for the analysis.

Table 2. Spectral and spatial resolution of the Sentinel 2A MSI bands (* denotes bands not considered in study.).

Sentinel-2 MSI Bands	Spatial Resolution (m)	Central Wavelength (nm)	Band Width (nm)
Band 1: Coastal Aerosol (b01) *	60	443	20
Band 2: Blue (b02)	10	490	65
Band 3: Green (b03)	10	560	35
Band 4: Red (b04)	10	665	30
Band 5: Vegetation Red Edge (b05)	20	705	15
Band 6: Vegetation Red Edge (b06)	20	740	15
Band 7: NIR (b07)	20	783	20
Band 8: NIR (b08)	10	842	115
Band 8A: NIR (b8a)	20	865	20
Band 9: Water Vapor (b09) *	60	945	20
Band 10: SWIR Cirrus (b10) *	60	1375	30
Band 11: SWIR (b11)	20	1610	90
Band 12: SWIR (b12)	20	2190	180

In addition, six spectral indices were considered (Table 3). The indices were based on the conventional normalized vegetation index (NDVI) that is computed as the difference between NIR and red reflectance divided by their sum, and the normalized burn ratio (NBR) that is computed as the difference between NIR and SWIR reflectance divided by their sum. Four NDVI variants derived at 10 m and at 20 m using the four different possible combinations and spatial resolutions of the red, red edge, and NIR bands were considered. Similarly, two NBR variants derived at 20 m using the 20 m NIR band and the two 20 m SWIR bands were considered.

Table 3. Spectral indices (denoted by the two bands used) considered in this study.

Spectral Index	Spatial Resolution (m)	Formulation
Normalized Difference Vegetation Index (8/4)	10	(b08 − b04) / (b08 + b04)
Normalized Difference Vegetation Index red-edge (8a/5)	20	(b8a − b05) / (b8a + b05)
Normalized Difference Vegetation Index red-edge (8a/6)	20	(b8a − b06) / (b8a + b06)
Normalized Difference Vegetation Index (8a/7)	20	(b8a − b07) / (b8a + b07)
Normalized Burn Ratio (8a/11)	20	(b8a − b11) / (b8a + b11)
Normalized Burn Ratio (8a/12)	20	(b8a − b12) / (b8a + b12)

3. Method

3.1. Burned and Unburned Pixel Sample Collection

For each pair of site images (Table 1) unambiguous pixel samples that were unburned in the first acquisition and burned in the second acquisition at the same geographic location were selected (termed for brevity unburned-burned class samples). In addition, to act as a control, unambiguous pixel samples that were unburned in the first and second acquisitions at the same geographic location (termed for brevity unburned-unburned class samples) were also selected. The control pixel locations

were different to the unburned-burned pixel locations but were selected nearby and over the same first acquisition vegetation types. The MSI spectral band (Table 2) and spectral index (Table 3) values were extracted at the selected pixel locations.

The burned and unburned pixel sample selection was undertaken interactively by an experienced geospatial analyst. True color 10 m (b04, b03, b02) and false color 20 m (b12, b11, b8a) TOA reflectance images for the two acquisitions were displayed. Image-processing software that allowed zooming, local contrast stretching, and rapid image comparison was used. The use of two date image pairs provides several interpretative advantages over single date data. It ensures that burned areas that occurred before the first acquisition date are not mistakenly mapped as having burned between the two acquisition dates, reduces the likelihood of spectral confusion with spectrally similar surfaces (e.g., water bodies or dark soil), and allows relative changes to be assessed [27,50,51]. Only pixels that were judged visually to be unaffected by cloud, optically thick smoke or haze, and that were shadow free were selected. In addition, to reduce burned area edge effects and the impact of any multi-temporal image misregistration, only pixels that were more than 20 m from a burned area edge were selected. To reduce the mapping effort, particularly in the sites containing large numbers of small and spatially fragmented burns, a minimum mapping unit of 60 m was adopted, whereby only burned areas with small axis dimensions of 60 m or greater were selected. To ensure the samples from both 10 m and 20 m spatial resolution images were for approximately the same locations, the geographic coordinates of the 20 m sample pixels were extracted first and then reconciled to the 10 m images. At each site, the unburned to burned class and the unburned to unburned class sample sizes were purposefully set to be similar. More than 8000 10 m and 2000 20 m samples were selected at each site (Table 4).

Table 4. Number of pairs of unburned (first image acquisition) to burned (second image acquisition) pixel samples and number of pairs of unburned (first image acquisition) to unburned (second image acquisition) pixel samples at 10 m resolution selected at each site. The total summed pixel areas in km^2 are shown in parentheses.

Site Location	Unburned to Burned	Unburned to Unburned
Australia, Northern Territory, near Fish River Block Gorge National Park	8056 (0.81)	8612 (0.86)
Cambodia, Kratié region, near Snoul	8072 (0.81)	8360 (0.84)
Canada, Alberta, Fort McMurray	15,692 (1.57)	14,124 (1.41)
Guinea, Faranah Prefecture, Parc National du Haut Niger	8616 (0.86)	8428 (0.84)
Colombia, Casanare Department, northern side of the Rio Cravo Sur river	8316 (0.83)	10,384 (1.04)

3.2. Statistical Separability Analysis

Parametric and non-parametric statistical measures were used to quantify the unburned-burned class separability for the different MSI bands (Table 2) and for the different spectral indices (Table 3) at each of the five sites. As a control, the unburned-unburned class separability was also quantified. The MSI bands and spectral indices with higher unburned-burned separability were considered more suitable for burned area mapping, particularly if their separability was greater than the unburned-unburned class separability.

3.2.1. Parametric Separability Analysis

The parametric transformed divergence (TD) separability measure was used. The TD is a commonly used measure that is bounded between values of 0 (no separability) and 2 (completely

separable) [52]. It provides a covariance weighted distance between class means to determine whether class signatures are separable as:

$$TD = 2\left[1 - \exp\left(-\frac{D}{8}\right)\right],$$

$$D = \frac{1}{2}tr\left[(C_1 - C_2)\left(C_1^{-1} - C_2^{-1}\right)\right] + \frac{1}{2}tr\left[\left(C_1^{-1} - C_2^{-1}\right)(\mu_1 - \mu_2)(\mu_1 - \mu_2)^T\right] \tag{1}$$

where TD is the transformed divergence between class *1* and class *2*, C_1 is the covariance matrix of class *1*, μ_1 is the mean vector of class *1*, *tr* is the matrix trace function, and *T* is the matrix transposition function. In this study, class *1* was defined by the unburned pixel samples from the first image acquisition and class *2* was defined by the corresponding burned samples from the second image acquisition (i.e., unburned-burned pairs). For the control group, classes *1* and *2* were defined from the unburned pixels from the first and second image acquisitions (i.e., unburned-unburned pairs). The rationale of the TD is to define the separation between two normal distributions (characterized by their mean vectors and covariance matrices), but most metrics used do not follow a Gaussian distribution [53]. In this respect, the TD is only indicative in cases of normality, or when classifiers based on the assumption of normality (e.g., maximum likelihood) are used. Consequently, the Shapiro-Wilk normality test [54] was used to assess if the unburned and burned pixel values were normally distributed. There are several normality tests but the Shapiro–Wilk test is considered to be reliable [55,56]. The test is best applied with small sample size less than 5000 and with a test null-hypothesis that the sample is drawn from a normally distributed population [57]. As there were typically more than 5000 unburned or burned pixel values at each site (Table 4) the Shapiro-Wilk test *p*-value was computed independently ten times, each time drawing 1000 values at random. This was undertaken for the unburned (first image acquisition) and burned (second image acquisition) pixel samples at each site and for each MSI band (Table 2) and spectral index (Table 3).

3.2.2. Non-Parametric Separability Analysis

In the last decade, the satellite land cover classification research community has moved away from the use of probability distribution classification approaches in favor of non-parametric approaches [58]. In particular, decision trees, and variants such as random forest, have attracted considerable attention as they can accommodate non–monotonic and nonlinear relationships between predictor variables and make no assumptions concerning the statistical distributions of the variables [59,60]. They also provide measures of the relative importance of the predictor variables in explaining the classification. However, decision tree and random forest predictor variable importance measures are inappropriate if the predictor variables are correlated [61,62], which certainly is the case for the different MSI bands and derived spectral band ratios considered in this study.

A bagged decision tree classification of the class samples was undertaken considering each MSI band and spectral index independently. Two hundred decision trees were grown, each time using 20% of the training samples selected randomly with replacement. After each tree was generated, the remaining "out-of-bag" 80% was classified with the tree and the classified "out-of-bag" results were stored as a vector of class labels. The majority class label over the 200 vectors was assigned as the classification result for each unique "out-of-bag" sample. These data were used to generate a two-way confusion matrix and conventional overall accuracy and Kappa measures were derived from the confusion matrix [63].

The overall accuracy (oa) is defined as the proportion of the pixels that are classified correctly and is calculated as:

$$oa = \frac{\sum X_{ii}}{n} \tag{2}$$

where X_{ii} is the element in row *i* and column *i* in the confusion matrix, and the confusion matrix is defined as a cross-tabulation of the counts of correctly classified and misclassified classes as Table 5:

Table 5. Cross-tabulation of the counts of correctly classified and misclassified classes.

		Reference Data	
		Class *1*	**Class *2***
Classified Data	**Class *1***	X_{11}	X_{12}
	Class 2	X_{21}	X_{22}

where *n* is the total number of samples classified $n = X_{11} + X_{12} + X_{21} + X_{22}$. The Kappa coefficient quantifies (under certain sampling assumptions) how much better, or worse, the classifier is than would be expected due to random chance and is bounded from 0 (very poor classification) to 1 (perfect classification) and is calculated as:

$$\kappa = \frac{p_0 - p_e}{1 - p_e} \qquad (3)$$

where p_0 is accuracy of observed agreement defined as $\frac{\sum X_{ii}}{n}$, p_e is the estimate of chance agreement defined as $\frac{\sum X_{i+} X_{+i}}{n^2}$, where X_{i+} is the sum of row *i*, and X_{+i} is the sum of column *i* in the confusion matrix. As for the TD separability analysis, these measures (Equations (2) and (3)) were derived with class *1*, defined by the unburned pixel samples from the first image acquisition, and class *2*, defined by the corresponding burned samples from the second image acquisition (i.e., unburned-burned pairs), and then again, as a control, considering classes *1* and *2* as the unburned pixels from the first and second image acquisitions respectively (i.e., unburned-unburned pairs).

4. Results

Figure 1 illustrates the mean reflectance and spectral index values of the unburned (first image acquisition) and burned (second image acquisition) pixel samples at each site. As discussed in the introduction, the impact of burning is predominantly to reduce NIR and SWIR reflectance. Among the spectral indices the NBR index derived from bands 8a and 12 (denoted b8a/12 in Figure 1) has the greatest mean unburned to burned reduction. Among the four NDVI band variants the greatest reductions occur for the 10m NDVI band (denoted 8/4 in Figure 1). These results should be treated with some caution as although a large number of pixels were considered (Table 4, middle column) the burned and unburned data were not normally distributed. This is illustrated in Figure 2 which shows the results of the Shapiro-Wilk normality tests. Only the unburned NDVI red edge band values (denoted 8a/6 and 8a/7 in Figure 2) for the Australia and Canada sites were significantly normally distributed, and only the burned NDVI red edge band derived from bands 8a and 7 for the Australia and Cambodia sites were significantly normally distributed.

The pattern of results in Figures 1 and 2 was similar for the atmospherically corrected (i.e., surface reflectance) data. To illustrate the effect of atmospheric correction, and provide context for the separability results, Figure 3 shows TOA and surface reflectance for the second image acquisition near Fort McMurray, Alberta, Canada, illustrating true color 10 m (b04, b03, b02) and false color 20 m (b12, b11, b8a) TOA and surface reflectance. The impact of the atmospheric correction is most apparent comparing the true color TOA reflectance (a) and surface reflectance (b). The atmospheric correction increases the true color image spatial contrast and reduces the blue appearance, which is expected from comparable Landsat atmospheric correction experiments [64,65]. The distinct smoke plume is not well corrected, which as noted earlier is a problem for most atmospheric correction methods. The impact of the atmospheric correction is visually less apparent in the longer wavelength false color bands, i.e., comparing (c) and (d), which is expected as atmospheric effects are smaller at longer wavelengths [65,66]. The false color longer wavelength bands are more sensitive to the effects of fire on vegetation and consequently the extensive burned area in the east side of the image has more contrast with the surrounding unburned vegetation than is apparent in the true color images. These qualitative results illustrate the need for careful band selection for burned area mapping.
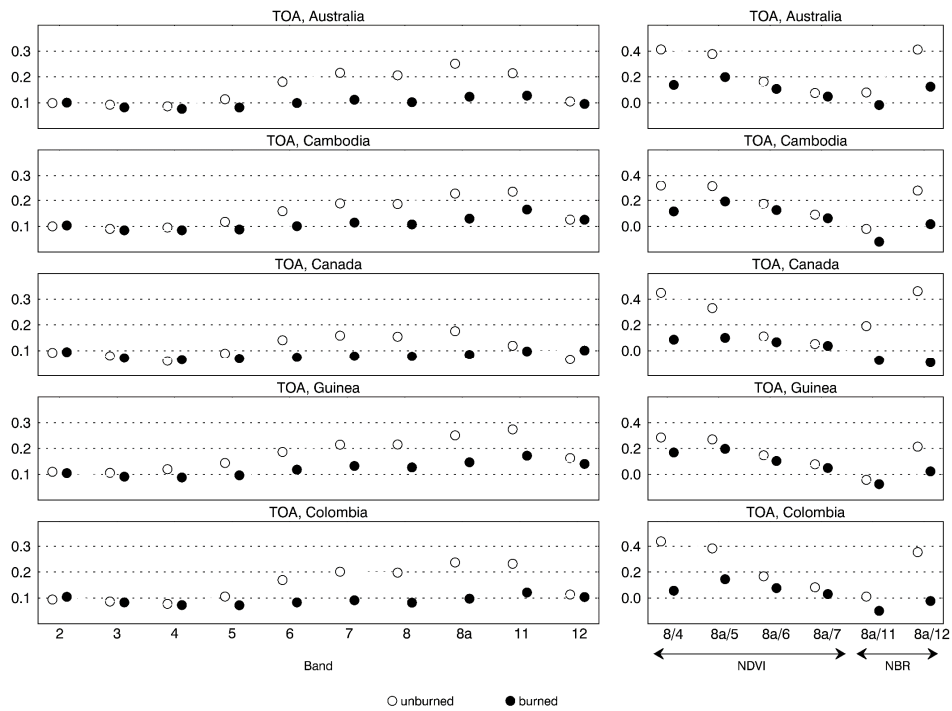
Figure 1. Mean unburned and burned MSI band (Table 2) and spectral index (Table 3) top of atmosphere (TOA) values.
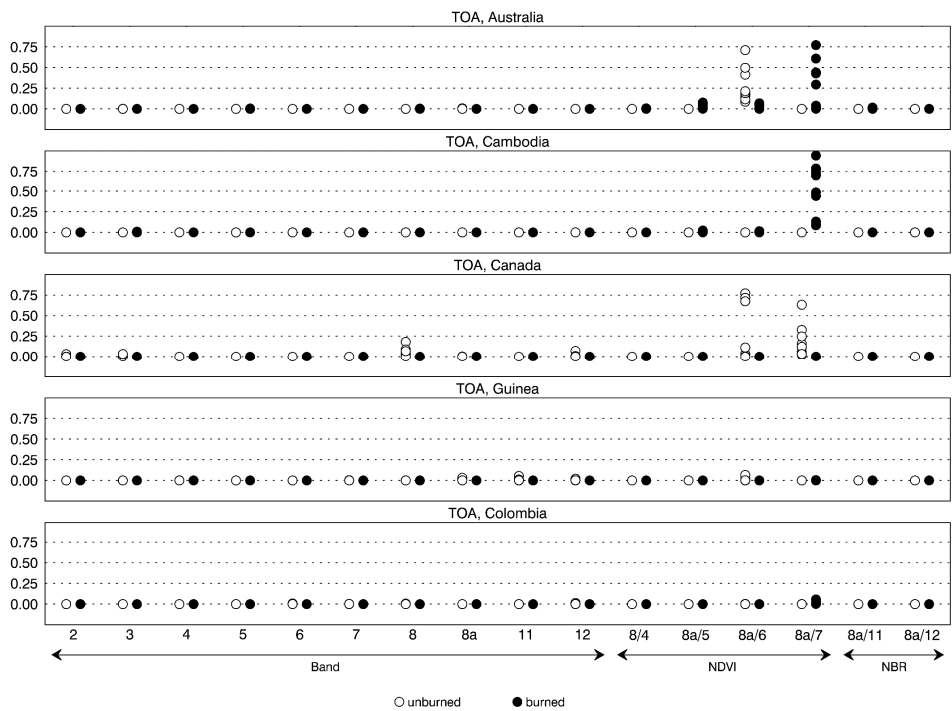

Figure 2. Shapiro-Wilk normality test *p*-values for the top of atmosphere (TOA) unburned and burned MSI band (Table 2) and spectral index values (Table 3). High *p*-values indicate that the null hypothesis that the data came from a normally distributed population cannot be rejected, i.e., that the data are normally distributed.
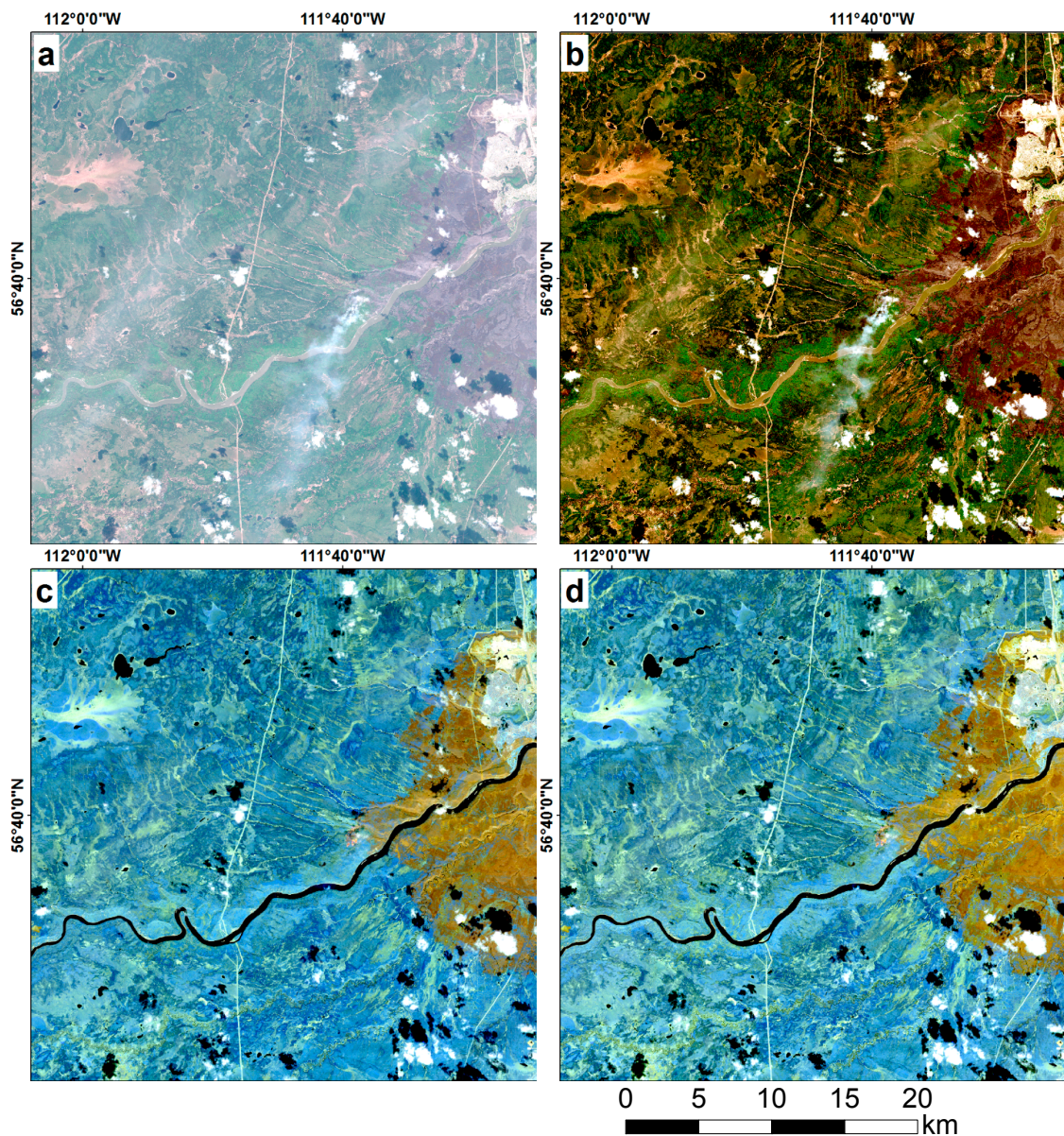
Figure 3. Example 40×40 km^2 pixel subset of the second Sentinel-2A MSI Canada image acquisition (12 May 2016) (**a**) true color (b04, b03, b02) 10 m top of atmosphere reflectance; and (**b**) SEN2COR atmospherically corrected equivalent bands displayed with the same logarithmic contrast stretch; (**c**) false color (b12, b11, b8a) 20 m top of atmosphere reflectance; and (**d**) SEN2COR atmospherically corrected equivalent bands displayed with the same contrast stretch.

Figure 4 illustrates the TD separability values for each of the TOA band reflectances and spectral indices. The blue bars illustrate the control unburned-unburned TD values and the red bars illustrate the unburned-burned TD values. Figure 5 shows the same results for the SEN2COR atmospherically corrected data. The impact of the atmosphere at visible wavelengths, i.e., for b02, b03 and b04, is apparent with greater differences between the TOA control (blue) and the unburned-burned (red) separability values (Figure 4) than for the equivalent TD surface (Figure 5) values. This reduction is much less apparent for the longer wavelength bands, because, as illustrated in Figure 3, the atmosphere has less effect at longer wavelengths. Residual atmospheric contamination may remain in the SEN2COR generated surface reflectance, particularly at shorter wavelengths [66].
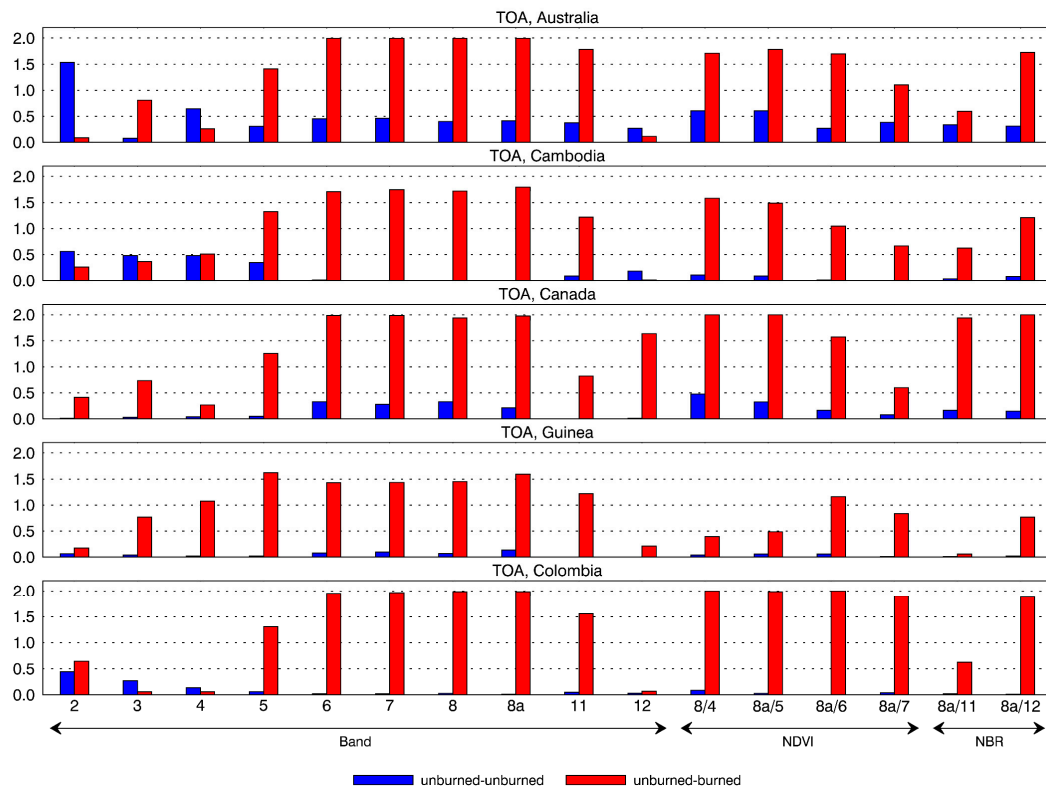
Figure 4. Transformed divergence (TD) top of atmosphere (TOA) separability values for the ten MSI bands (Table 2) and the six spectral indices (Table 3).
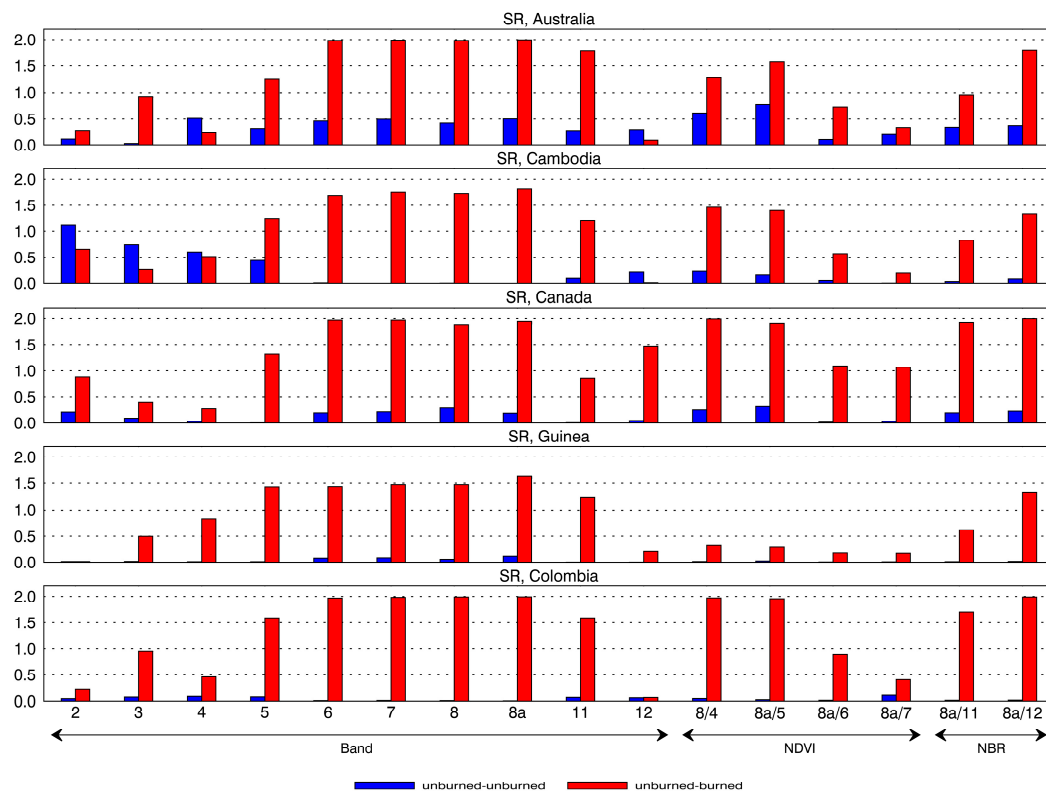

Figure 5. Transformed divergence (TD) separability values as Figure 4 but derived from the surface reflectance data (i.e., from the SEN2COR atmospherically corrected data).

With regard to the unburned to unburned control pixels, the separability for each band and spectral index is generally quite low. This is expected because the images were acquired 10 or 20 days apart and so change in the surface condition (e.g., vegetation state and soil moisture changes) at the unburned pixel locations is likely to be small. With regard to the unburned to burned pixels, a clear TD separability pattern among the different bands and indices is evident. This pattern is similar to the decision tree classification results. As noted previously, the TD is indicative of class separability if probability distribution classification approaches (i.e., maximum likelihood) are used and if the data are normally distributed. As the data are not normally distributed (Figure 2), the decision tree kappa and overall accuracy results provide a more precise depiction of class separability, and these are discussed below.

Figures 6 and 7 illustrate the decision tree separability results for the TOA and the SEN2COR atmospherically corrected data respectively. In these two figures the overall accuracy and kappa values are very similar (across the ten bands and six indices the values are highly correlated with r > 0.98 for both the illustrated TOA and surface reflectance results). The surface unburned-burned kappa and overall accuracy values are always higher than the control unburned-unburned equivalent values (Figure 7) which is expected. This is also the case for the TOA results (Figure 6) except for the blue band over Australia, due to strong atmospheric effects in the shortest wavelength blue band.
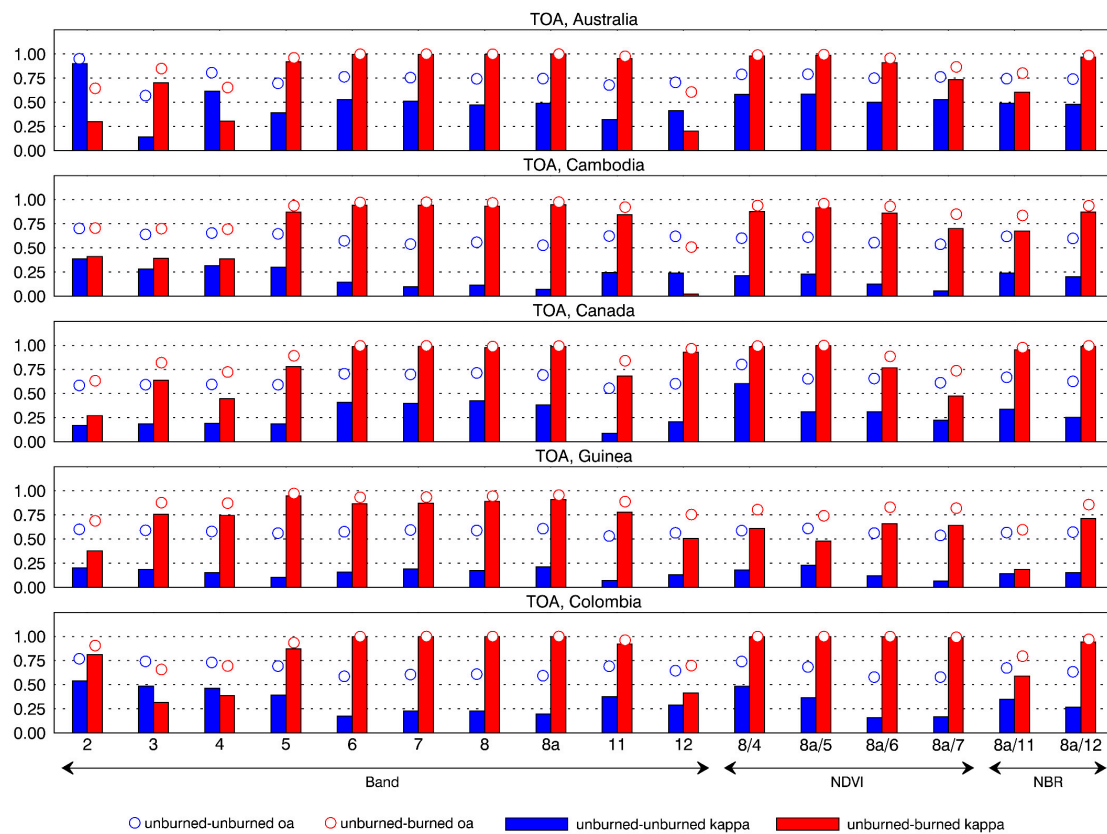

Figure 6. Decision tree top of atmosphere (TOA) separability values for the ten MSI bands (Table 2) and the six spectral indices (Table 3). Overall accuracy values are shown as circles and Kappa values are shown as bars.
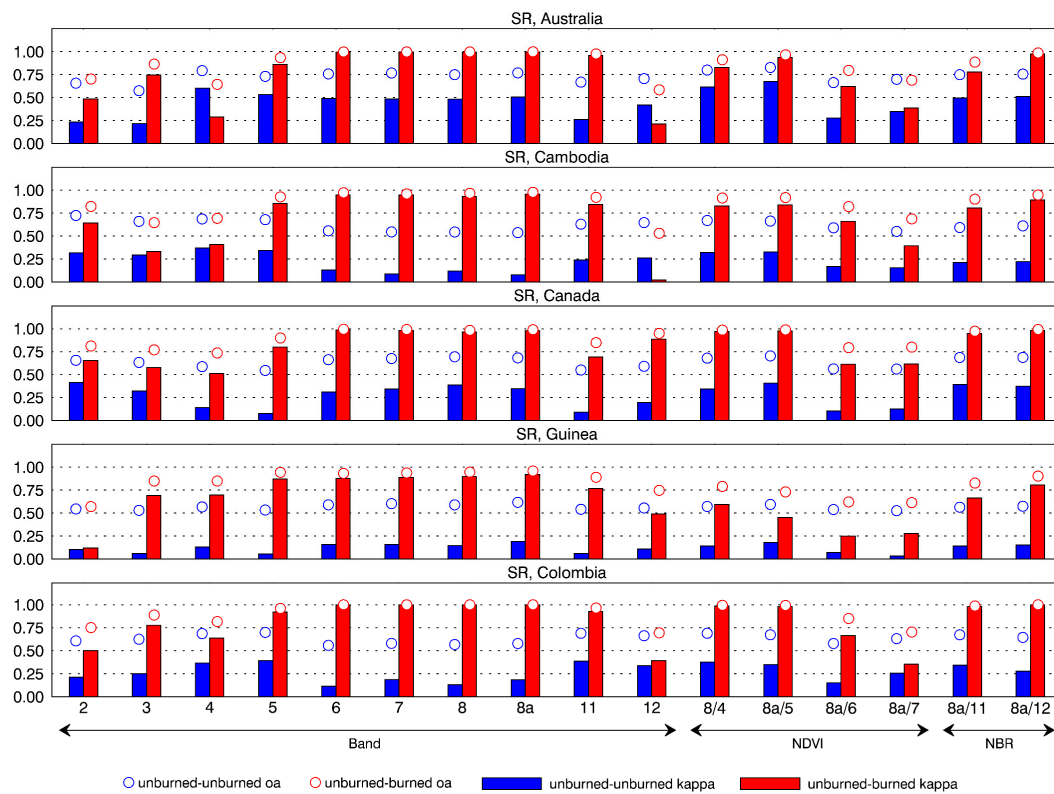
Figure 7. Decision tree separability values as Figure 6 but derived from the surface reflectance data (i.e., from the SEN2COR atmospherically corrected data).

Considering the ten different MSI bands, the visible bands (b02, b03, b04) have the lowest unburned-burned separability (both overall accuracy and kappa) for all the sites (Figures 6 and 7). The longest wavelength MSI band (b12: 2190 nm) also has low separability, except for the Canadian site TOA and surface reflectance where the burned reflectance was much higher than the unburned vegetation which has been observed by others for boreal and temperate forested regions [17,36,67]. High overall accuracy (>0.8) and kappa (>0.8) values are found for the red-edge (b05, b06), NIR (b07, b08, b08a) and the SWIR (b11: 1610 nm) bands. It is well established that the NIR has high burned-unburned separability due primarily to the greater NIR reflectance of green and dry vegetation compared to black char [15,23,68,69]. The high SWIR band burned-unburned separability is less established, and, for example, has been found to vary geographically [23] and is suggested by some researchers as being related to the removal of water-retaining vegetation post-fire that leads to an increase in SWIR reflectance [70–72]. The high red-edge band burned-unburned separability, particularly evident for b06 (740 nm), is of great interest as this band is not present on most spaceborne sensors. The red-edge bands are included on the MSI primarily because they have potential for vegetation chlorophyll content retrieval [73,74]. For all five sites, fire resulted in a decrease in the red-edge band reflectance values, perhaps due to the removal of vegetation, and so reduced canopy chlorophyll content, in addition to decreased reflectance due to black char deposition.

The four NDVI spectral indices provide variable among-site separability. This is expected and, for example, NDVI is observed to provide poor burned-unburned discrimination over dry senescent vegetation but reasonable discrimination over boreal forest [23,71]. The TOA and surface NDVI separability values are particularly low over the Guinea site where the predominant vegetation type is woody savanna. We note that the Guinea acquisitions were in the local dry season, and other researchers have observed that the NDVI of unburned and burned dry senescent savanna vegetation is quite similar [75–77]. For the non-Guinea sites moderate to high separability values are found for the 10 m NDVI (denoted 8/4 in Figures 6 and 7) and for the 20 m NDVI derived from b8a and b05 (denoted

8a/5 in Figures 6 and 7). The other two NDVI implementations are defined at 20 m (b8a/6 and b8a/7) and have relatively lower separability, perhaps because they have the closest wavelength separation between their red and NIR bands. Among all the sites there is no clear pattern comparing the TOA and surface reflectance derived NDVI separability values. This in part is because the impact of the atmosphere on NDVI varies as function of the background red and NIR reflectance; with typically a greater increase in NDVI when imagery is atmospherically corrected over vegetated rather than over soil dominated surfaces [65]. The two 20 m NBR indices (denoted 8A/11 and 8A/12 in Figures 4–7), like the NDVI, have variable among site separability values. However, for all the sites, the NBR implementation derived from b08 and b12 provides comparable or higher separability than the NDVI values and supports the broad adoption of the NBR for burned area mapping.

5. Discussion

This study provides an evaluation of the effectiveness of individual Sentinel-2A MSI bands and spectral indices for discriminating burned areas. It supports the findings of previous studies that the NIR provides high burned-unburned discrimination in a variety of ecosystems including, for example, boreal forest [23,78,79], savanna [23,75,80] and temperate forest [36]. As observed in other studies, the visible bands provide low burned-unburned discrimination [23,75,81,82]. This is primarily because the visible reflectance spectra of non-photosynthetic vegetation is similar to the spectra of burned vegetation and also to soil that may be revealed post-fire [12,21,83]. Few studies have considered the red-edge wavelength region for burned area mapping because it is not present on sensors commonly used for fire monitoring. The two MSI red-edge bands demonstrated relatively high burned-unburned discrimination and this was previously observed using Medium Resolution Imaging Spectroradiometer (MERIS) data [84]. Given the performance of the Sentinel-2 MSI red edge bands, which will also be present on the Sentinel-3 Ocean and Land Colour Instrument (OLCI) sensor [74], the results of this study suggest they could be combined, for example, by an efficient model inversion [85].

The performance of the NDVI and NBR spectral indices considered in this study was not generally comparable with the better performing spectral bands in the sense that the spectral index separabilities were more variable among the five sites. The majority of previous studies concerning the suitability of spectral indices for burned area mapping have been specific to a given biome or land cover type. As stated in [71,86] (boreal forest), [77] (savanna), [87] (grass-shrub), the performance of NDVI is limited by vegetation senescence or growth, and the NDVI has been shown to provide poor discrimination in savannas [75–77]. The NBR was developed originally for burned area mapping [33], and not for satellite-based assessments of fire/burn severity although it is used widely for this purpose [88–91]. The MSI NBR provided comparable or higher separability than the NDVI and the NBR has been observed by others to provide high burned-unburned discriminative capability, e.g., [33] (mediterranean forest), [34] (boreal forest), [80] (savanna), [92] (heathland). The reported separabilities for the spectral indices were likely more variable among the five sites than for the individual bands because the spectral indices combine bands from spectral regions with different sensitivities to factors including the vegetation type and condition, the soil background, atmospheric contamination, and the degree of char and ash deposition [14]. Therefore, caution in the interpretation of the exact cause of the different separability results is necessary, particularly given the complexity of the post-fire surface trajectory discussed in the introduction.

This study only considered the effectiveness of individual Sentinel-2A MSI bands and spectral indices for discriminating burned areas in a radiometric sense. Further work to consider the relative advantages of the 10 m bands, particularly the 10 m NIR band, for improved spatial resolution burned area mapping is recommended, although we note that the 20 m and 10 m bands have different wavelengths and so are not directly comparable. Burned area mapping algorithms usually take advantage of the discriminative power of multiple spectral bands, for example, by thresholding spectral indices. In this study, we reported separability analyses in the conventional manner with respect to single indices and bands. This provides meaningful insights into which individual indices

and bands are appropriate for burned area mapping. The effective use of multiple bands and/or indices for burned area mapping is dependent on the algorithm used. The design of algorithm-specific experiments is beyond the scope of this study, but is a recommended subject for future research.

The unburned and burned MSI reflectance and derived spectral index values were generally not normally distributed indicating that parametric separability measures, such as the transformed divergence or the Jeffries-Matusita distance [52], are less appropriate for analyses of the sort reported in this study. The decision tree based non-parametric separability approach that we used is straightforward and easily implementable. However, issues related to the unburned and burned sample data collection, the atmospheric correction, and the global representativeness of the image data used, may reduce the generality of the reported findings. The sample data were collected through interactive visual interpretation of two date image pairs. Only unambiguously burned and unburned pixels were collected. Albeit unlikely, it is not possible to exclude the presence of misinterpreted samples. This is difficult to avoid and quantify, but given the large sample sizes this issue is not expected to be significant. The sample data were collected in images unaffected by strong atmospheric contamination. Furthermore, the SEN2COR atmospheric correction may have its own limitations. Therefore, the findings are less likely to be representative of particularly smoke or atmospherically contaminated Sentinel-2 MSI data. Finally, the collection of moderate resolution image pairs in a statistically robust way that represent global fire conditions is subject to ongoing research [51]. It is unknown if the study findings would be significantly different if the analysis was undertaken using more sites and image pairs acquired at different times in the local fire season.

6. Conclusion

Spectral separability analysis was undertaken to examine the ability of Sentinel-2A MSI data to detect fire-induced spectral change, which is both a challenging and an important task for burned area mapping. It is evident that Sentinel-2A MSI data can provide spectral differentiation between unburned and burned classes. The NDVI derived from the 10 m and 20 m red and NIR bands, and the NBR derived from the 20 m NIR and SWIR bands, provided variable discriminative ability. Individual 20 m NIR, red-edge, and SWIR bands were most sensitive to the change in reflectance caused by fire. These findings are similar to other studies undertaken using different sensors and data. To date, burned area mapping has been undertaken over large areas using coarser than 20 m resolution data. The findings reported in this study suggest the potential and need for further research to develop a systematic Sentinel-2A MSI 20 m burned area mapping capability.

Author Contributions: Haiyan Huang undertook the data analysis, and processed the data with help from Hankui K. Zhang, Jian Li, Lin Yan, Sanath Sathyachandran Kumar, and developed the graphics with assistance from Hankui K. Zhang and David P. Roy; David P. Roy structured and drafted the manuscript with assistance from Haiyan Huang, Luigi Boschetti, and Jose Gomez-Dans.

Conflicts of Interest: The authors declare no conflict of interest.

References

1. Giglio, L.; Descloitres, J.; Justice, C.O.; Kaufman, Y.J. An enhanced contextual fire detection algorithm for MODIS. *Remote Sens. Environ.* **2003**, *87*, 273–282. [CrossRef]

2. Roy, D.P.; Boschetti, L.; Justice, C.O.; Ju, J. The collection 5 MODIS burned area product-Global evaluation by comparison with the MODIS active fire product. *Remote Sens. Environ.* **2008**, *12*, 3690–3707. [CrossRef]

3. Xu, W.; Wooster, M.J.; Roberts, G.; Freeborn, P. New GOES imager algorithms for cloud and active fire detection and fire radiative power assessment across North, South and Central America. *Remote Sens. Environ.* **2010**, *114*, 1876–1895. [CrossRef]

4. Zhang, X.; Kondragunta, S.; Ram, J.; Schmidt, C.; Huang, H.C. Near real time global biomass burning emissions product from geostationary satellite constellation. *Geophys. Res. Atmos.* **2012**. [CrossRef]

5. Mouillot, F.; Schultz, M.G.; Yue, C.; Cadule, P.; Tansey, K.; Ciais, P.; Chuvieco, E. Ten years of global burned area products from spaceborne remote sensing—A review: Analysis of user needs and recommendations for future developments. *Int. J. Appl. Earth Obs. Geoinf.* **2014**, *26*, 64–79. [CrossRef]

6. Schroeder, W.; Oliva, P.; Giglio, L.; Csiszar, I.A. The new VIIRS 375 m active fire detection data product: Algorithm description and initial assessment. *Remote Sens. Environ.* **2014**, *143*, 85–96. [CrossRef]

7. Alonso-Canas, I.; Chuvieco, E. Global burned area mapping from ENVISAT-MERIS and MODIS active fire data. *Remote Sens. Environ.* **2015**, *163*, 140–152. [CrossRef]

8. Boschetti, L.; Roy, D.P.; Justice, C.O.; Humber, M.L. MODIS–Landsat fusion for large area 30 m burned area mapping. *Remote Sens. Environ.* **2015**, *161*, 27–42. [CrossRef]

9. Drusch, M.; Del Bello, U.; Carlier, S.; Colin, O.; Fernandez, V.; Gascon, F.; Hoersch, B.; Isola, C.; Laberinti, P.; Martimort, P. Sentinel-2: ESA's optical high-resolution mission for GMES operational services. *Remote Sens. Environ.* **2012**, *120*, 25–36. [CrossRef]

10. Pereira, J.M.C. Remote sensing of burned areas in tropical savannas. *Int. J. Wildland Fire* **2003**, *12*, 259–270. [CrossRef]

11. Trigg, S.N.; Roy, D.P.; Flasse, S.P. An in situ study of the effects of surface anisotropy on the remote sensing of burned savannah. *Int. J. Remote Sens.* **2005**, *26*, 4869–4876. [CrossRef]

12. Roy, D.P.; Boschetti, L.; Maier, S.W.; Smith, A.M.S. Field estimation of ash and char color-lightness using a standard gray scale. *Int. J. Wildland Fire* **2010**, *19*, 698–704. [CrossRef]

13. Lentile, L.B.; Holden, Z.A.; Smith, A.M.S.; Falkowski, M.J.; Hudak, A.T.; Morgan, P.; Lewis, S.A.; Gessler, P.E.; Benson, N.C. Remote sensing techniques to assess active fire characteristics and post-fire effects. *Int. J. Wildland Fire* **2006**, *15*, 319–345. [CrossRef]

14. Roy, D.P.; Landmann, T. Characterizing the surface heterogeneity of fire effects using multi-temporal reflective wavelength data. *Int. J. Remote Sens.* **2005**, *26*, 4197–4218. [CrossRef]

15. Pereira, J.M.C.; Chuvieco, E.; Beaudoin, A.; Desbois, N. Remote sensing of burned areas: A review. In *A Review of Remote Sensing Methods for The Study of Large Wildland Fire Report of The Megafires Project ENV-CT96-0256*; Chuvieco, E., Ed.; Universidad de Alcala: Alcala de Henares, Spain, 1997; pp. 127–183.

16. Trigg, S.N.; Flasse, S.P. Characterizing the spectral-temporal response of burned savannah using in situ spectroradiometry and infrared thermometry. *Int. J. Remote Sens.* **2000**, *21*, 3161–3168. [CrossRef]

17. Fraser, R.H.; Li, Z.; Landry, R. SPOT VEGETATION for characterizing boreal forest fires. *Int. J. Remote Sens.* **2000**, *21*, 3525–3532. [CrossRef]

18. Jin, Y.; Roy, D.P. Fire-induced albedo change and its radiative forcing at the surface in northern Australia. *Geophys. Res. Lett.* **2005**, *32*, L13401. [CrossRef]

19. Vila, J.P.S.; Barbosa, P. Post-fire vegetation regrowth detection in the Deiva Marina region (Liguria-Italy) using Landsat TM and ETM+ data. *Ecol. Model.* **2010**, *221*, 75–84. [CrossRef]

20. Chu, T.; Guo, X.; Takeda, K. Remote sensing approach to detect post-fire vegetation regrowth in Siberian boreal larch forest. *Ecol. Indic.* **2016**, *62*, 32–46. [CrossRef]

21. Smith, A.M.S.; Wooster, M.J.; Drake, N.A. Testing the potential of multi-spectral remote sensing for retrospectively estimating fire severity in African Savannahs. *Remote Sens. Environ.* **2005**, *97*, 92–115. [CrossRef]

22. Stroppiana, D.; Pinnock, S.; Pereira, J.M.C.; Grégoire, J.-M. Radiometric analysis of SPOT-VEGETATION images for burnt area detection in Northern Australia. *Remote Sens. Environ.* **2002**, *82*, 21–37. [CrossRef]

23. Roy, D.P.; Jin, Y.; Lewis, P.E.; Justice, C.O. Prototyping a global algorithm for systematic fire-affected area mapping using MODIS time series data. *Remote Sens. Environ.* **2005**, *97*, 137–162. [CrossRef]

24. Kaufman, Y.J.; Hobbs, P.V.; Kirchhoff, V.W.J.H.; Artaxo, P.; Remer, L.A.; Holben, B.N.; King, M.D.; Ward, D.E.; Prins, E.M.; Longo, K.M.; et al. Smoke, Clouds, and Radiation-Brazil (SCAR-B) experiment. *J. Geophys. Res. Atmos.* **1998**, *103*, 31783–31808. [CrossRef]

25. Lyapustin, A.; Wang, Y.; Laszlo, I.; Kahn, R.; Korkin, S.; Remer, L.; Levy, R.; Reid, J.S. Multiangle implementation of atmospheric correction (MAIAC): 2. Aerosol algorithm. *J. Geophy. Res. Atmos.* **2011**. [CrossRef]

26. Verstraete, M.M.; Pinty, B. Designing optimal spectral indexes for remote sensing applications. *IEEE Trans. Geosci. Remote Sens.* **1996**, *34*, 1254–1265. [CrossRef]

27. Chuvieco, E.; Martín, M.P.; Palacios, A. Assessment of different spectral indices in the red-near-infrared spectral domain for burned land discrimination. *Int. J. Remote Sens.* **2002**, *23*, 5103–5110. [CrossRef]

28. Chuvieco, E.; Riaño, D.; Danson, F.M.; Martin, P. Use of a radiative transfer model to simulate the postfire spectral response to burn severity. *J. Geophys. Res. Biogeosci.* **2006**. [CrossRef]

29. Levin, N.; Heimowitz, A. Mapping spatial and temporal patterns of Mediterranean wildfires from MODIS. *Remote Sens. Environ.* **2012**, *126*, 12–26. [CrossRef]

30. Fernandez-Manso, A.; Fernandez-Manso, O.; Quintano, C. SENTINEL-2A red-edge spectral indices suitability for discriminating burn severity. *Int. J. Appl. Earth Obs. Geoinf.* **2016**, *50*, 170–175. [CrossRef]

31. Liu, W.; Wang, L.; Zhou, Y.; Wang, S.; Zhu, J.; Wang, F. A comparison of forest fire burned area indices based on HJ satellite data. *Nat. Hazards* **2016**, *81*, 971–980. [CrossRef]

32. Gao, F.; Jin, Y.; Schaaf, C.B.; Strahler, A.H. Bidirectional NDVI and atmospherically resistant BRDF inversion for vegetation canopy. *IEEE Trans. Geosci. Remote Sens.* **2002**, *40*, 1269–1278.

33. Garcia, M.J.L.; Caselles, V. Mapping burns and natural reforestation using thematic Mapper data. *Geocarto Int.* **1991**, *6*, 31–37. [CrossRef]

34. Loboda, T.; O'Neal, K.; Csiszar, I. Regionally adaptable dNBR-based algorithm for burned area mapping from MODIS data. *Remote Sens. Environ.* **2007**, *109*, 429–442. [CrossRef]

35. Stroppiana, D.; Boschetti, M.; Zaffaroni, P.; Brivio, P. Analysis and interpretation of spectral indices for soft multicriteria burned-area mapping in mediterranean regions. *IEEE Geosci. Remote Sens. Lett.* **2009**, *6*, 499–503. [CrossRef]

36. Veraverbeke, S.; Harris, S.; Hook, S. Evaluating spectral indices for burned area discrimination using MODIS/ASTER (MASTER) airborne simulator data. *Remote Sens. Environ.* **2011**, *115*, 2702–2709. [CrossRef]

37. Davies, D.K.; Ilavajhala, S.; Wong, M.M.; Justice, C.O. Fire information for resource management system: Archiving and distributing MODIS active fire data. *IEEE Trans. Geosci. Remote Sens.* **2009**, *47*, 72–79. [CrossRef]

38. Giglio, L.; Csiszar, I.; Justice, C.O. Global distribution and seasonality of active fires as observed with the Terra and Aqua Moderate Resolution Imaging spectroradiometer (MODIS) sensors. *J. Geophys. Res. Biogeosci.* **2006**. [CrossRef]

39. Friedl, M.A.; Sulla-Menashe, D.; Tan, B.; Schneider, A.; Ramankutty, N.; Sibley, A.; Huang, X. MODIS Collection 5 global land cover: Algorithm refinements and characterization of new datasets. *Remote Sens. Environ.* **2010**, *114*, 168–182. [CrossRef]

40. Roy, D.P.; Li, J.; Zhang, H.K.; Yan, L. Best practices for the reprojection and resampling of Sentinel-2 Multi Spectral Instrument Level 1C data. *Remote Sens. Lett.* **2016**, *7*, 1023–1032. [CrossRef]

41. Yan, L.; Roy, D.P.; Zhang, H.; Li, J.; Huang, H. An automated approach for sub-pixel registration of Landsat-8 Operational Land Imager (OLI) and Sentinel-2 Multi Spectral Instrument (MSI) imagery. *Remote Sens.* **2016**, *8*, 520. [CrossRef]

42. Languille, F.; Déchoz, C.; Gaudel, A.; Greslou, D.; de Lussy, F.; Trémas, T.; Poulain, V. Sentinel-2 geometric image quality commissioning: First results. *Proc. SPIE* **2015**. [CrossRef]

43. Coppin, P.; Jonckheere, I.; Nackaerts, K.; Muys, B.; Lambin, E. Digital change detection methods in ecosystem monitoring: A review. *Int. J. Remote Sens.* **2004**, *25*, 1565–1596. [CrossRef]

44. Kaufman, Y.J.; Sendra, C. Algorithm for automatic corrections to visible and near IR satellite imagery. *Int. J. Remote Sens.* **1988**, *9*, 1357–1381. [CrossRef]

45. Tanre, D.; Herman, M.; Deschamps, P.Y. Influence of the background contribution upon space measurements of ground reflectance. *Appl. Opt.* **1981**, *20*, 3676–3684. [CrossRef] [PubMed]

46. Chavez, P.S., Jr. Image-based atmospheric correction—Revisited and improved. *Photogramm. Eng. Remote Sens.* **1996**, *62*, 1025–1036.

47. Müller-Wilm, U. *Sentinel-2 MSI-Level-2A Prototype Processor Installation and User Manual*; Telespazio VEGA Deutschland GmbH: Darmstadt, Germany, 2015.

48. Claverie, M.; Vermote, E.; Franch, B.; He, T.; Hagolle, O.; Kadiri, M.; Masek, J. Evaluation of medium spatial resolution BRDF-Adjustment techniques using multi-angular SPOT4 (Take5) acquisitions. *Remote Sens.* **2015**, *7*, 12057–12075. [CrossRef]

49. Roy, D.P.; Zhang, H.K.; Ju, J.; Gomez-Dans, J.L.; Lewis, P.E.; Schaaf, C.B.; Sun, Q.; Li, J.; Huang, H.; Kovalskyy, V. A general method to normalize Landsat reflectance data to nadir BRDF adjusted reflectance. *Remote Sens. Environ.* **2016**, *176*, 255–271. [CrossRef]

50. Roy, D.P.; Frost, P.; Justice, C.; Landmann, T.; Le Roux, J.; Gumbo, K.; Makungwa, S.; Dunham, K.; Du Toit, R.; Mhwandagara, K.; et al. The Southern Africa Fire Network (SAFNet) regional burned area product validation protocol. *Int. J. Remote Sens.* **2005**, *26*, 4265–4292. [CrossRef]

51. Boschetti, L.; Stehman, S.V.; Roy, D.P. A stratified random sampling design in space and time for regional to global scale burned area product validation. *Remote Sens. Environ.* **2016**, *186*, 465–478. [CrossRef]

52. Jensen, J.R. *Introductory Digital Image Processing: A Remote Sensing Perspective*, 2nd ed.; Prentice Hall: Upper Saddle River, NJ, USA, 1996.

53. Egorov, A.V.; Hansen, M.C.; Roy, D.P.; Kommareddy, A.; Potapov, P.V. Image interpretation-guided supervised classification using nested segmentation. *Remote Sens. Environ.* **2015**, *165*, 135–147. [CrossRef]

54. Shapiro, S.S.; Wilk, M.B. An analysis of variance test for normality (complete samples). *Biometrika* **1965**, *52*, 591–611. [CrossRef]

55. Mendes, M.; Pala, A. Type I error rate and power of three normality tests. *Pak. J. Inform. Technol.* **2003**, *2*, 135–139.

56. Razali, N.M.; Wah, Y.B. Power comparisons of shapiro-wilk, kolmogorov-smirnov, lilliefors and anderson-darling tests. *J. Stat. Model. Anal.* **2011**, *2*, 21–33.

57. Royston, P. Remark AS R94: A remark on algorithm AS181: The W-test for normality. *J. R. Stat. Soc. Ser.* **1995**, *44*, 547–551.

58. Gómez, C.; White, J.C.; Wulder, M.A. Optical remotely sensed time series data for land cover classification: A review. *ISPRS J. Photogramm. Remote Sens.* **2016**, *116*, 55–72. [CrossRef]

59. Breiman, L. Bagging predictors. *Mach. Learn.* **1996**, *24*, 123–140. [CrossRef]

60. Breiman, L. Random forests. *Mach. Learn.* **2001**, *45*, 5–32. [CrossRef]

61. Hothorn, T.; Hornik, K.; Zeileis, A. Unbiased recursive partitioning: A conditional inference framework. *J. Comput. Graph. Stat.* **2006**, *15*, 651–674. [CrossRef]

62. Strobl, C.; Boulesteix, A.L.; Kneib, T.; Augustin, T.; Zeileis, A. Conditional variable importance for random forests. *BMC Bioinform.* **2008**. [CrossRef] [PubMed]

63. Foody, G.M. Status of land cover classification accuracy assessment. *Remote Sens. Environ.* **2002**, *80*, 185–201. [CrossRef]

64. Ouaidrari, H.; Vermote, E.F. Operational atmospheric correction of Landsat TM data. *Remote Sens. Environ.* **1999**, *70*, 4–15. [CrossRef]

65. Roy, D.P.; Qin, Y.; Kovalskyy, V.; Vermote, E.F.; Ju, J.; Egorov, A.; Hansen, M.C.; Kommareddy, I.; Yan, L. Conterminous United States demonstration and characterization of MODIS-based Landsat ETM+ atmospheric correction. *Remote Sens. Environ.* **2014**, *140*, 433–449. [CrossRef]

66. Ju, J.; Roy, D.P.; Vermote, E.; Masek, J.; Kovalskyy, V. Continental-scale validation of MODIS-based and LEDAPS Landsat ETM+ atmospheric correction methods. *Remote Sens. Environ.* **2012**, *122*, 175–184. [CrossRef]

67. Van Wagtendonk, J.W.; Root, R.R.; Key, C.H. Comparison of AVIRIS and Landsat ETM+ detection capabilities for burn severity. *Remote Sens. Environ.* **2004**, *92*, 397–408. [CrossRef]

68. Koutsias, N.; Karteris, M. Logistic regression modelling of multitemporal Thematic Mapper data for burned area mapping. *Int. J. Remote Sens.* **1998**, *19*, 3499–3514. [CrossRef]

69. Pereira, J.M.; Sá, A.C.; Sousa, A.M.; Silva, J.M.; Santos, T.N.; Carreiras, J.M. Spectral characterisation and discrimination of burnt areas. In *Remote Sensing of Large Wildfires*; Springer: Berlin, Germany, 1999; pp. 123–138.

70. White, J.D.; Ryan, K.C.; Key, C.C.; Running, S.W. Remote sensing of forest fire severity and vegetation recovery. *Int. J. Wildland Fire* **1996**, *6*, 125–136. [CrossRef]

71. Fraser, R.H.; Li, Z.; Cihlar, J. Hotspot and NDVI differencing synergy (HANDS): A new technique for burned area mapping over boreal forest. *Remote Sens. Environ.* **2000**, *74*, 362–376. [CrossRef]

72. He, L.; Chen, J.M.; Zhang, S.; Gomez, G.; Pan, Y.; McCullough, K.; Masek, J.G. Normalized algorithm for mapping and dating forest disturbances and regrowth for the United States. *Int. J. Appl. Earth Obs. Geoinf.* **2011**, *13*, 236–245. [CrossRef]

73. Dash, J.; Curran, P.J. The MERIS terrestrial chlorophyll index. *Int. J. Remote Sens.* **2004**, *25*, 5403–5413. [CrossRef]

74. Clevers, J.G.; Gitelson, A.A. Remote estimation of crop and grass chlorophyll and nitrogen content using red-edge bands on Sentinel-2 and -3. *Int. J. Appl. Earth Obs. Geoinf.* **2013**, *23*, 344–351. [CrossRef]

75. Roy, D.P.; Lewis, P.E.; Justice, C.O. Burned area mapping using multi-temporal moderate spatial resolution data—A bi-directional reflectance model-based expectation approach. *Remote Sens. Environ.* **2002**, *83*, 263–286. [CrossRef]

76. Eva, H.; Lambin, E.F. Burnt area mapping in Central Africa using ATSR data. *Int. J. Remote Sens.* **1998**, *19*, 3473–3497. [CrossRef]

77. Trigg, S.; Flasse, S. An evaluation of different bi-spectral spaces for discriminating burned shrub-savannah. *Int. J. Remote Sens.* **2001**, *22*, 2641–2647. [CrossRef]

78. Chu, T.; Guo, X. Compositing MODIS time series for reconstructing burned areas in the Taiga–Steppe transition zone of northern Mongolia. *Int. J. Wildland Fire* **2015**, *24*, 419–432. [CrossRef]

79. Fraser, R.H.; Li, Z. Estimating fire-related parameters in boreal forest using SPOT VEGETATION. *Remote Sens. Environ.* **2002**, *82*, 95–110. [CrossRef]

80. Smith, A.M.S.; Drake, N.A.; Wooster, M.J.; Hudak, A.T.; Holden, Z.A.; Gibbons, C.J. Production of Landsat ETM+ reference imagery of burned areas within Southern African savannahs: comparison of methods and application to MODIS. *Int. J. Remote Sens.* **2007**, *28*, 2753–2775. [CrossRef]

81. Lasaponara, R. Estimating spectral separability of satellite derived parameters for burned areas mapping in the Calabria region by using SPOT-Vegetation data. *Ecol. Model.* **2006**, *196*, 265–270. [CrossRef]

82. Pereira, J.M.C. A comparative evaluation of NOAA/AVHRR vegetation indexes for burned surface detection and mapping. *IEEE Trans. Geosci. Remote Sens.* **1999**, *37*, 217–226. [CrossRef]

83. Asner, G.P.; Heidebrecht, K.B. Spectral unmixing of vegetation, soil and dry carbon cover in arid regions: Comparing multispectral and hyperspectral observations. *Int. J. Remote Sens.* **2002**, *23*, 3939–3958. [CrossRef]

84. Oliva, P.; Martín, P.; Chuvieco, E. Burned area mapping with MERIS post-fire image. *Int. J. Remote Sens.* **2011**, *32*, 4175–4201. [CrossRef]

85. Gomez-Dans, J.L.; Lewis, P.E.; Disney, M. Efficient emulation of radiative transfer codes using Gaussian processes and application to land surface parameter inferences. *Remote Sens.* **2016**, *8*, 119. [CrossRef]

86. Zhang, Y.H.; Wooster, M.J.; Tutubalina, O.; Perry, G.L.W. Monthly burned area and forest fire carbon emission estimates for the Russian Federation from SPOT VGT. *Remote Sens. Environ.* **2003**, *87*, 1–15. [CrossRef]

87. Rogan, J.; Yool, S.R. Mapping fire-induced vegetation depletion in the Peloncillo Mountains Arizona and New Mexico. *Int. J. Remote Sens.* **2001**, *22*, 3101–3121. [CrossRef]

88. Cocke, A.E.; Fule, P.Z.; Crouse, J.E. Comparison of burn severity assessments using differenced normalized burn ratio and ground data. *Int. J. Wildland Fire* **2005**, *14*, 189–198. [CrossRef]

89. Epting, J.; Verbyla, D.; Sorbel, B. Evaluation of remotely sensed indices for assessing burn severity in interior Alaska using Landsat TM and ETM+. *Remote Sens. Environ.* **2005**, *96*, 328–339. [CrossRef]

90. Roy, D.; Boschetti, L.; Trigg, S. Remote sensing of fire severity: Assessing the performance of the normalized burn ratio. *IEEE Geosci. Remote Sens. Lett.* **2006**, *3*, 112–116. [CrossRef]

91. French, N.H.; Kasischke, E.S.; Hall, R.J.; Murphy, K.A.; Verbyla, D.L.; Hoy, E.E.; Allen, J.L. Using Landsat data to assess fire and burn severity in the North American boreal forest region: An overview and summary of results. *Int. J. Wildland Fire* **2008**, *17*, 443–462. [CrossRef]

92. Schepers, L.; Haest, B.; Veraverbeke, S.; Spanhove, T.; Vanden Borre, J.; Goossens, R. Burned area detection and burn severity assessment of a heathland fire in Belgium using Airborne Imaging Spectroscopy (APEX). *Remote Sens.* **2014**, *6*, 1803–1826. [CrossRef]